# Ice sheet-free West Antarctica during peak early Oligocene glaciation

*J. P. Klages[1]*, C.-D. Hillenbrand[2], S. M. Bohaty[3], U. Salzmann[4], K. Gohl[1], T. Bickert[5], G. Lohmann[1,5,6], H. S. Knahl[1], P. Gierz[1], L. Niu[1], J. Titschack[5,7], G. Kuhn[1,8], T. Frederichs[5,8], J. Müller[1,5,8], T. Bauersachs[9], R. D. Larter[2], K. Hochmuth[10], W. Ehrmann[11], G. Nehrke[1], F. J. Rodríguez-Tovar[12], G. Schmiedl[13], S. Spezzaferri[14], A. Läufer[15], F. Lisker[8], T. van de Flierdt[16], A. Eisenhauer[17], G. Uenzelmann-Neben[1], O. Esper[1], J. A. Smith[2], H. Pälike[5,8], C. Spiegel[8], R. Dziadek[1], T. A. Ronge[18], and T. Freudenthal[5]*

[1] Alfred-Wegener-Institut Helmholtz-Zentrum für Polar- und Meeresforschung, Bremerhaven, Germany
[2] British Antarctic Survey, Cambridge, United Kingdom
[3] Institute of Earth Sciences, University of Heidelberg, Heidelberg, Germany
[4] Department of Geography and Environmental Sciences, Northumbria University, Newcastle upon Tyne, United Kingdom
[5] MARUM – Center for Marine Environmental Sciences, Bremen, Germany
[6] Environmental Physics, University of Bremen, Bremen, Germany
[7] Marine Research Department, Senckenberg am Meer (SAM), Wilhelmshaven, Germany
[8] Faculty of Geosciences, University of Bremen, Bremen, Germany
[9] Chair of Organic Biogeochemistry in Geo-Systems, RWTH Aachen University, Aachen, Germany
[10] Australian Centre for Excellence in Antarctic Science, Institute for Marine & Antarctic Studies, University of Tasmania, Hobart, Australia
[11] Institute for Geophysics and Geology, University of Leipzig, Leipzig, Germany
[12] Departamento de Estratigrafía y Paleontología, Universidad de Granada, Granada, Spain
[13] Center for Earth System Research and Sustainability, Institute for Geology, University of Hamburg, Hamburg, Germany
[14] Department of Geosciences, University of Fribourg, Fribourg, Switzerland
[15] Polar Geology, Bundesanstalt für Geowissenschaften und Rohstoffe, Hannover, Germany
[16] Department of Earth Science & Engineering, Imperial College London, London, United Kingdom
[17] GEOMAR Helmholtz-Zentrum für Ozeanforschung Kiel, Kiel, Germany
[18] International Ocean Discovery Program, Texas A&M University, College Station, TX, USA

* Corresponding author: Johann.Klages@awi.de

One sentence summary

Highly asymmetric initial Antarctic glaciation 34 Ma ago reveals differential Antarctic Ice Sheet response to fundamental climatic change.

**One of Earth's most fundamental climate shifts – the greenhouse-icehouse transition 34 Ma ago – initiated Antarctic ice-sheet build-up, influencing global climate until today. However, the extent of the ice sheet during the Early Oligocene Glacial Maximum (~33.7–33.2 Ma) that immediately followed this transition, a critical knowledge gap for assessing feedbacks between permanently glaciated areas and early Cenozoic global climate reorganization, is uncertain. Here, we present shallow-marine drilling data constraining earliest Oligocene environmental conditions on West Antarctica's Pacific margin – a key region for understanding Antarctic ice sheet-evolution. These data indicate a cool-temperate environment, with mild ocean and air temperatures preventing West Antarctic Ice Sheet formation. Climate-ice sheet modeling corroborates a highly asymmetric Antarctic ice sheet, thereby revealing its differential regional response to past and future climatic change.**

Plausible projections of future transitions into very different climate states require a profound understanding of the dynamics of drastic climate changes in Earth's past. One such fundamental change – i.e., from early Cenozoic greenhouse to late Cenozoic icehouse conditions – occurred across the Eocene-Oligocene Transition (EOT) and is evident from a sharp, two-step increase of deep ocean oxygen isotope ($\delta^{18}O$) values reflecting a combination of both decreasing but regionally highly variable ocean temperatures and major ice sheet build-up (*1–4*). The first $\delta^{18}O$ step occurred during the EOT (~34.4–33.7 Ma) (*1–3*), thought to be initiated by low summer insolation (*3*), while the second, more prominent step – known as the 'Early Oligocene oxygen Isotope Step' (EOIS) (*4*) and commonly referred to as 'Oi-1' (*1, 3*) – marks the end of the EOT and the start of the Early Oligocene Glacial Maximum (EOGM; ~33.7–33.2 Ma) (*1, 5*). Constraints on the size, location, and timing of growth of early Antarctic ice sheets, however, remain sparse (*6–8*), preventing us from assessing their impact on past global climate dynamics, including ice–ocean–atmosphere interactions during phases of substantial change (*2*).

In the Northern Hemisphere, previous studies inferred patches of marine-terminating land-based ice on Greenland already during the mid–late Eocene from the deposition of ice-rafted debris (IRD) in the Norwegian-Greenland Sea (*9*), but without firm constraints on ice-mass size and location. In contrast, East Antarctic land-based ice likely grew stepwise throughout the EOT – starting from late Eocene ephemeral alpine glaciation to glacial advance towards outer shelf regions in Prydz Bay (*10*), with further evidence for contemporary iceberg rafting in both the adjacent deep sea (*11*) and the Weddell Sea region (*11, 12*). In the Ross Sea sector, presence of grounded ice directly at the coast has not been documented before ~33 Ma (*13*). For West Antarctica, it is debated whether there was major ice sheet build-up during the EOT–EOGM (*6, 14, 15*) or later during the late Oligocene–early Miocene interval (*16*). Numerical models suggest that the prominent EOIS at ~33.7 Ma (*4*) is best explained by Antarctic glaciation alone, likely with a partial (*17*) or full (*7*) West Antarctic contribution. So far, however, reliable records proximal to West Antarctica that could document the presence or absence of a West Antarctic Ice Sheet (WAIS) during the EOGM are missing.

Here we report on drill core records from the West Antarctic margin that reveal paleoenvironmental conditions during the EOGM. Site PS104_21 (73.31°S, 107.11°W; 882 m water depth; Fig. 1) was drilled during RV *Polarstern* expedition PS104 in Pine Island Trough on the Amundsen Sea Embayment (ASE) shelf (*18*), with two holes (21-2 and 21-3) ~86 m apart. Seaward-dipping strata beneath the mid-shelf part of the trough are truncated near the seafloor by an amalgamated unconformity caused by repeated Miocene–Pleistocene cross-shelf ice advances (*19–21*) (Fig. 1b). These sedimentary strata were shown to be of mid-Cretaceous age at the inner–mid shelf transition (*20*) and become successively younger in a seaward direction (*18*). However, the semi-lithified character of the dipping sequences previously prevented their recovery with conventional coring methods. This hurdle was overcome by deploying the MARUM-MeBo70 seafloor drill rig (*22*), which allowed drilling ~10 m into the seabed and sampling of the dipping, semi-lithified strata (*18*) (Figs. 1, 2).

**Lithology and stratigraphy**

Beneath a thin layer of late Quaternary sediments, laminated semi-lithified muds and mudstones, interrupted by three intervals of no recovery (Fig. 2), extend to the bottom of the ~10 m deep hole 21-3. These strata contain both terrestrial and marine microfossils but lack any gravel-sized grains and bear only traces of terrigenous sand (Fig. 2). A ~4 m thick sequence of identical semi-lithified muds and mudstones was retrieved in hole 21-2, which we correlated to hole 21-3 using lithological features and magnetic susceptibility data (Fig. S1). The presence of distinct, mostly horizontally-oriented trace fossils without cross-cutting relationships and absence of mottling throughout hole 21-3 indicate abundant epi- and shallow endobenthic life while excluding significant vertical bioturbation of the sedimentary record by

infauna (Movie S1). Thin sections were prepared from two carbonate-cemented mudstone beds at ~8.78–8.74 meters below seafloor (mbsf) and ~3.33–3.23 mbsf (Fig. 2), which contain rare calcareous microfossils, such as benthic foraminifera, and indistinct microscopic fragments of terrestrial organic matter. Five samples taken within the laminated mudstone interval provided sufficient biogenic carbonate for radiogenic strontium (Sr) isotope stratigraphic dating (Fig. 2; Table S1), consistently returning latest Eocene to earliest Oligocene ages between 34.59 ±0.2 Ma and 33.09 ±0.2 Ma, with a mean age of 33.82 ±0.18 Ma (Fig. S2). Likely due to minor diagenetic alteration and/or syndepositional reworking from shallower seabed, these $^{87}Sr/^{86}Sr$ dates show no clear stratigraphic order but most of them overlap within error. Based on the tight cluster of the $^{87}Sr/^{86}Sr$ ages from both above and below a magnetic reversal recorded at the top of core 3R (Fig. 2), this transition from reversed to normal polarity is correlated to the boundary between magnetic polarity chrons C13r and C13n at 33.73 Ma (*23*), which corresponds to the EOIS (*4*, *24*) (Fig. S2). This correlation to the geomagnetic polarity timescale is also supported by present *Bolboforma* species *B. indistincta* and *B. irregularis*, which have last and first occurrences within calcareous nannofossil zone NP21 that spans the EOT and EOGM (*25*).

**Paleoenvironment and climate**

Sediment cores 5R to 1R from hole PS104_21-3 (Fig. 2) and cores 3R and 2R from hole 21-2 (Fig. S1) (*26, 27*) record a marine environment evident from rare but continuous occurrences of both marine microfossils (i.e., foraminifera, dinoflagellate cysts, calcareous nannofossils, and *Bolboforma*; Table S2; Fig. S3) and trace fossils (e.g., *Zoophycos*; Movie S1). Dominance of benthic foraminifera, with only one planktic specimen found (Table S2), designate a relatively shallow (50–200 m) mid- to outer-shelf environment (*28*), consistent with the presence of *Bolboforma* – an extinct group of calcareous microfossils – previously also described from water depths as shallow as 30–50 m (*29*). Similar benthic foraminiferal and *Bolboforma* assemblages have so far only been reported from the early Oligocene of the Victoria Land Basin (*28*) and the late Eocene/Oligocene from the eastern Australian margin (*25*), respectively. The dominance of epifaunal to shallow-infaunal benthic foraminifera species and trace fossils (Table S2; Movie S1) indicates well-ventilated bottom waters but reduced oxygen penetration into the seabed, likely due to the extremely fine grain size of the sediments (Fig. 2). The benthic foraminiferal assemblage additionally points to pulses of phytodetritus and frequent influx of freshwater (*28*). This is also supported by elevated ratios of terrestrial versus aquatic-sourced short-chain hydrocarbons (*30*) ($TAR_{HC}$; Fig. 2), suggesting increased influx of terrestrial organic matter (TOM) from vegetated land, as does the presence of the trace fossil *Phycosiphon incertum* (*31*). Comparatively high Branched and Isoprenoid Tetraether (BIT) index values of >0.5 (Fig. 2) indicate that TOM influx has mainly been facilitated by rivers and creeks (*32*) (Fig. 1). A close proximity to land is further indicated by the regular occurrence of pollen and spores of higher land plants (Fig. 2; Table S3). Low alkane $n\text{-}C_{31}/(n\text{-}C_{27}+n\text{-}C_{29}+n\text{-}C_{31})$ ratios point to prevalent deciduous trees (*30*) (Fig. S4).

The fossil pollen assemblage in our record (Fig. S11; Table S3) closely resembles modern pollen rain spectra from the South American subantarctic deciduous forest biome (*33*), characterized by very high percentages (>80–90%; Table S4) of *Nothofagidites* pollen (Nearest Living Relative; NLR: *Nothofagus*; see Table S5) and regular occurrences of conifer pollen (NLR: *Podocarpus, Microcachryidites antarcticus, Araucariaceae)* and *Stereosporites* (NLR: *Sphagnum* mosses). Today, such southern beech-rich forests are abundant in Patagonia, where they thrive in a cool-temperate climate with mean annual air temperatures of ~6.0–8.5°C, mean summer temperatures of ~9.8–13.8°C, and a mean annual precipitation of >1,500 mm (*33*). These vegetation-derived terrestrial temperatures are in close accordance with our $TEX^{L}_{86}$ sub-surface ocean temperatures (SOT) of the archipelago, which range from ~6.2°C to ~10.5°C (±2.8°C calibration error; Figs. 2, 3). Comparatively high BIT and ΔRI values may additionally bias $TEX^{L}_{86}$-based temperature reconstructions, i.e., ±2.9°C in sediments receiving higher amounts of TOM

(see 'Materials and Methods' in Supplementary Materials for applying the $TEX^{L}86$ calibration despite high BIT values). The occasional dissolution of resistant *Bolboforma* specimens (Fig. S3d–f) indicates that seawater temperatures may have periodically dropped to 5°C or less throughout the year (*34*). In general, those temperatures would have been too high to allow any presence of permanent marine-terminating ice. Moreover, the predominance of subangular to rounded quartz grains in the sand fraction throughout the PS104_21 record, including grains with shiny surfaces and medium to high sphericities (Fig. 2), argues against their glacial erosion and subglacial transport. Instead, these grain characteristics are more indicative of fluvial transport (*35*) on nearby land and thus corroborating our interpretation of the foraminiferal assemblage and BIT index. Furthermore, the lack of clastic grains >2 mm, commonly used as IRD proxy (*36*), in the fine-grained sediments at this location (Fig. 2) indicates that land-based ice was absent from the coastal region near the site. Additionally, very low contents of kaolinite (~5%; Fig. 2) may further support a WAIS-free scenario since subglacial erosion in the Byrd Subglacial Basin is considered to be the main source for kaolinite in modern and late Quaternary ASE sediments (*37*).

The PS104_21 record clearly documents a marine depositional setting, hence validating the minimum Antarctic bed topography reconstruction for 34 Ma proposed by ref. *38* for West Antarctica as opposed to their medium and maximum scenarios, in which the entire area around Site PS104_21 is land (*38*). Our findings suggest that parts of West Antarctica must have already been situated below sea level during the EOGM, potentially allowing the existence of open trans-Antarctic seaways (Fig. 1). This interpretation is supported by recent findings of reworked Paleogene open ocean microfossils in modern subglacial sediments from the Siple and Gould coasts in the Ross Sea sector (*39*). Overall, we infer that during peak early Oligocene glaciation the coasts of West Antarctica's Amundsen Sea sector were still covered by cool-temperate forests without evidence for marine-terminating ice. Hence, any large permanent West Antarctic ice mass must have been very distant or did not exist until after the EOGM, implying that deep-sea cooling may have had a larger impact on the EOGM $\delta^{18}O$ signature in benthic foraminifera than previously thought.

**Paleoenvironmental modelling**

Our data constraints contradict results of previous model simulations that included a fully-developed, marine-terminating WAIS during the EOGM (~2x PI $CO_2$) (*3, 7*) (Fig. 3) and support model outputs implying limited West Antarctic ice coverage (*40*). However, available models differ considerably in simulating the amount of ice (*7, 17, 40, 41*), mainly because of the scarcity of field data and associated uncertainties in bed topography reconstructions (*38*). Here, we use the state-of-the-art Alfred Wegener Institute-Earth System Model (AWI-ESM-2.1-LR) asynchronously coupled to the Parallel Ice Sheet Model (PISM) (see 'Materials and Methods' in Supplementary Materials) to further explore the consequences of a vegetated and ice sheet-free West Antarctica we reconstructed for the EOGM. AWI-ESM-2.1-LR consists of fully coupled atmosphere, ocean, and sea ice components (*42*), supplemented by the land-surface and vegetation module JSBACH. The asynchronously coupled experiment was run into quasi-equilibrium state (1,500 climate years and 200,000 ice years, Fig. S5e–g). For our simulation, we used the reconstructed minimum bed topography (*38*) as a boundary condition (Fig. S5a) because only this reconstruction is consistent with our multi-proxy record from West Antarctica's Pacific margin.

Our multi-proxy evidence closes a critical West Antarctic gap in paleoenvironmental data for the earliest Oligocene (Fig. 3). In order to upscale the regional signal, we further combined our results with environmental data from other circum-Antarctic records spanning the earliest Oligocene interval (~33.9–31.0 Ma) (Fig. 3; Table S6). With that, we obtain an earliest Oligocene continent-wide context for comparing our EOGM ice sheet and climate reconstruction from site PS104_21 to climate model results. We specifically ran our simulation with the reconstructed atmospheric $CO_2$ concentration of ~850 ppmv,

representing latest Eocene conditions just prior to the EOGM (*43*) (~3x pre-industrial [PI] $CO_2$; Fig. 4). Reconstructed surface air and ocean temperatures for the EOGM reveal a clear pattern with warmer conditions in the southwestern Pacific and along the Wilkes Land margin (Fig. 3). Considering the uncertainties for both temperature reconstructions (including analytical and calibration errors) and Earth-system modelling (e.g., gateway bathymetry, orbital configuration, deep water formation) at high latitudes, our compiled proxy temperature data for the earliest Oligocene (Fig. 3; Table S6) best match simulated temperatures that were initiated with 3x PI $CO_2$ conditions (~850 ppmv; Fig. 4b, c; Fig. S5). This is – within uncertainty – consistent with recently revised $CO_2$ reconstructions from marine proxies across the EOT, which average 800–1000 ppmv in the late Eocene and decrease to ~600 ppmv following the EOT (*43*), although neither the exact timing nor the exact $CO_2$ concentration of this minimum are well constrained. Under such climate conditions, our simulation is also consistent with earliest Oligocene data constraints on ice-sheet extent in Prydz Bay (*10*) and the western Ross Sea (*13, 44*) (Fig. 4a). However, importantly, our model simulates an ice sheet-free West Antarctica not only for 3x PI $CO_2$ but also for 2x PI $CO_2$ conditions (Fig. 4a, e). Both simulated scenarios therefore agree with our data interpretation from Site PS104_21 that West Antarctica remained ice sheet-free during the EOGM, and exhibit a West Antarctic biome (Fig. 4d; Fig. S7) that matches well with our reconstructed vegetation (Fig. 2) and climate. Moreover, the results predict a potential ice-sheet nucleus close to the coast of northern Victoria Land (Fig. S6d; see 'Materials and Methods' in Supplementary Materials) – near a location in the Ross Sea where geological evidence documents the presence of grounded ice as early as 33.0 Ma and its proximity since at least 33.3 Ma (*13, 44, 45*). This nucleus – in contrast to, e.g., the Gamburtsev Mountains in the continent's dry interior – was likely initiated by increased precipitation (Fig. S7) from moist air masses originating from warm waters that reached the rapidly uplifting and already >1,500–2,000 m-high Transantarctic Mountains (*46*) (Fig. 3; white arrows in Fig. S5) and possibly flowed through an open, but yet shallow, Tasman Gateway (*47*). This led to increased precipitation and prominent ice-cap formation over northern Victoria Land.

Overall, our model results imply that growth and expansion of a marine-terminating ice sheet in West Antarctica occurred much later than in East Antarctica (*10, 13*). Ice advances reaching the West Antarctic coast initiated only at lower atmospheric $CO_2$ levels between ~560 ppmv and 280 ppmv (Fig. S6a, b) – values first recorded after ~26 Ma in the late Oligocene (*43*), when Antarctica's thermal isolation had progressed further (*47*). For the EOGM, we calculate a total Antarctic ice volume between 1.66 and 1.45 x $10^7$ $km^3$ (38.0–32.5 m sea level equivalent) (Figs. 4a; S6b), which aligns with minimum volume estimates calculated from deep-sea foraminiferal $\delta^{18}O$ and Mg/Ca data for the EOGM interval (*5*). Marine-terminating ice advance in the Amundsen Sea sector was likely delayed by subdued topography as well as prevailing mild air and surface ocean temperatures in this region (as shown by our PS104_21 record) but was initiated earlier in the Ross Sea sector (Fig. S6a, b). In the ASE, warmer waters may have reached the low-lying archipelago from lower latitudes as a consequence of yet shallow configurations of both the Tasman Gateway and Drake Passage (*47*), which affected this area for much longer than assumed until recently (*48*). Hence, our climate–ice sheet simulation is entirely consistent with our well-dated multi-proxy record, which indicated an ice sheet-free West Antarctica throughout the EOGM. Strongly reduced ice-associated climate feedbacks, such as albedo, likely further helped maintaining regional warmth and associated circulation patterns in the atmosphere and ocean (*49*).

We conclude that a large but not continent-wide ice sheet existed only in East Antarctica during the initial phase of the Cenozoic icehouse. Our results match previous EOGM ice sheet volume estimates (*4, 5, 24*) and suggest initial WAIS expansion into marine basins when atmospheric $CO_2$ concentrations began to fall below ~560 ppmv, i.e., at least ~7 Myr later in the late Oligocene (*43*). Hence, our combined multi-proxy data and climate–ice sheet simulation reveal a highly asymmetric behavior of the Antarctic ice sheet,

providing essential insight for understanding its response during past and future climate reorganizations.

## References and Notes


1. J. Zachos, M. Pagani, L. Sloan, E. Thomas, K. Billups, Trends, rhythms, and aberrations in global climate 65 Ma to present. *Science* **292**, 686–693 (2001).
2. T. Westerhold, et al., An astronomically dated record of Earth's climate and its predictability over the last 66 million years. *Science* **369**, 1383–1387 (2020).
3. J. B. Ladant, Y. Donnadieu, V. Lefebvre, C. Dumas, The respective role of atmospheric carbon dioxide and orbital parameters on ice sheet evolution at the Eocene-Oligocene transition. *Paleoceanography* **29**, 810–823 (2014).
4. D. K. Hutchinson, et al., The Eocene–Oligocene transition: a review of marine and terrestrial proxy data, models and model-data comparisons. *Clim. Past* **17**, 269–315 (2021).
5. S. M. Bohaty, J. C. Zachos, M. L. Delaney, Foraminiferal Mg/Ca evidence for Southern Ocean cooling across the Eocene–Oligocene transition. *Earth Planet. Sci. Lett.* **317-318**, 251–261 (2012).
6. S. Galeotti, et al., Chapter 7 – The Eocene–Oligocene boundary climate transition: an Antarctic perspective. *In: Florindo, F., Siegert, M., De Santis, L. & Naish, T. (eds.) Antarctic Climate Evolution (Second Edition)*, Elsevier, 297–361 (2022).
7. D. S. Wilson, D. Pollard, R. M. DeConto, S. S. R. Jamieson, B. P. Luyendyk, Initiation of the West Antarctic Ice Sheet and estimates of total Antarctic ice volume in the earliest Oligocene. *Geophys. Res. Lett.* **40**, 4305–4309 (2013).
8. Z. Liu, et al., Global cooling during the Eocene–Oligocene climate transition. *Science* **323**, 1187–1190 (2009).
9. J. S. Eldrett, I. C. Harding, P. A. Wilson, E. Butler, A. P. Roberts, Continental ice in Greenland during the Eocene and Oligocene. *Nature* **446**, 176–179 (2007).
10. S. Passchier, D. J. Ciarletta, T. E. Miriagos, P. K. Bijl, S. M. Bohaty, An Antarctic stratigraphic record of stepwise ice growth through the Eocene–Oligocene transition. *GSA Bulletin* **129**, 318–330 (2017).
11. W. Ehrmann, A. Mackensen, Sedimentological evidence for the formation of an East Antarctic ice sheet in Eocene/Oligocene time. *Palaeogeogr. Palaeoclim. Palaeoecol.* **93**, 85–112 (1992).
12. A. Carter, T. R. Riley, C.-D. Hillenbrand, M. Rittner, Widespread Antarctic glaciation during the Late Eocene. *Earth Planet. Sci. Lett.* **458**, 49–57 (2017).
13. S. Galeotti, et al., Antarctic Ice Sheet variability across the Eocene–Oligocene boundary climate transition. *Science* **352**, 76–80 (2016).
14. S. A. Marenssi, S. Casadío, S. N. Santillana, Record of Late Miocene glacial deposits on Isla Marambio (Seymour Island), Antarctic Peninsula. *Ant. Sci.* **22**, 193–198 (2010).
15. L. C. Ivany, S. van Simaeys, E. W. Domack, S. D. Samson, Evidence for an earliest Oligocene ice sheet on the Antarctic Peninsula. *Geology* **34**, 377–380 (2006).
16. J. W. Marschalek, et al., A large West Antarctic Ice Sheet explains early Neogene sea-level amplitude. *Nature* **600**, 450–455 (2021).
17. R. M. DeConto, D. Pollard, P. A. Wilson, H. Pälike, C. H. Lear, M. Pagani, Thresholds for Cenozoic bipolar glaciation. *Nature* **455**, 652–656 (2008).
18. K. Gohl, et al., MeBo70 Seabed Drilling on a Polar Continental Shelf: Operational Report and Lessons from Drilling in the Amundsen Sea Embayment of West Antarctica. *Geochem. Geophys. Geosys.* **18**, 4235–4250 (2017).
19. A. L. Lowe, J. B. Anderson, Reconstruction of the West Antarctic ice sheet in Pine Island Bay during the Last Glacial Maximum and its subsequent retreat history. *Quat. Sci. Rev.* **21**, 1879– 1897 (2002).
20. J. P. Klages, et al., Temperate rainforests near the South Pole during peak Cretaceous warmth. *Nature* **580**, 81–86 (2020).
21. K. Gohl, et al., Seismic stratigraphic record of the Amundsen Sea Embayment shelf from pre- glacial to recent times: Evidence for a dynamic West Antarctic ice sheet. *Mar. Geol.* **344**, 115– 131 (2013).

22. T. Freudenthal, G. Wefer, Drilling cores on the sea floor with the remote-controlled sea floor drilling rig MeBo. *Geosci. Instrum. Methods Data Syst.* **2**, 329–337 (2013).
23. F. M. Gradstein, J. G. Ogg, M. Schmitz, G. Ogg, Geologic Time Scale 2020 – 1st Edition. Elsevier, doi:10.1016/C2020-1-02369-3 (2020).
24. L. Diester-Haass, R. Zahn, Eocene–Oligocene transition in the Southern Ocean: History of water mass circulation and biological productivity. *Geology* **24**, 163–166 (1996).
25. D. Spiegler, S. Spezzaferri, *Bolboforma* – an overview. *Paläontologische Zeitschrift* **79/1**, 167– 181 (2005).
26. J. P. Klages, et al., Palynological, palaeomagnetic, and sediment physical investigations of cores 1R to 3R from MARUM-MeBo70 Site PS104_21-2. PANGAEA, https://doi.org/10.1594/PANGAEA.940329.
27. J. P. Klages, et al., Sedimentological, palynological, geochemical, palaeomagnetic, geochronological, and sediment physical investigations of cores 1R to 5R from MARUM-MeBo70 Site PS104_21-3. PANGAEA, https://doi.org/10.1594/PANGAEA.940344.
28. C. P. Strong, P.-N. Webb, Lower Oligocene Foraminiferal Fauna from CRP-3 Drillhole, Victoria Land Basin, Antarctica. *Terra Ant.* **8**, 347–358 (2001).
29. C. W. Poag, A. L. Karowe, Stratigraphic potential of Bolboforma significantly increased by new finds in the North Atlantic and South Pacific. *PALAIOS* **1**, 162–171 (1986).
30. P. A. Meyers, Applications of organic geochemistry to paleolimnological reconstructions: A summary of examples from the Laurentian Great Lakes. *Org. Geochem.* **34**, 261–289 (2003).
31. F. J. Rodríguez-Tovar, J. Nagy, M. Reolid, Palaeoenvironment of Eocene prodelta in Spitsbergen recorded by the trace fossil *Phycosiphon incertum*. *Polar Res.* **33**, 23786 (2014).
32. E. C. Hopmans, et al., A novel proxy for terrestrial organic matter in sediments based on branched and isoprenoid tetraether lipids. *Earth Planet. Sci. Lett.* **224**, 107–116 (2004).
33. V. Montade, et al., A pollen–climate calibration from western Patagonia for palaeoclimatic reconstructions. *J. Quat. Sci.* **34**, 76–86 (2019).
34. J.-D. Naviaux, et al., Temperature dependence of calcite dissolution kinetics in seawater. *Geochim. Cosmochim. Acta* **246**, 363–384 (2019).
35. K. Vos, N. Vandenberghe, J. Elsen, Surface textural analysis of quartz grains by scanning electron microscopy (SEM): From sample preparation to environmental interpretation. *Earth-Sci. Rev.* **128**, 93–104 (2014).
36. H. Grobe, A simple method for the determination of ice-rafted debris in sediment cores. *Polarforschung* **57**, 123–126 (1987).
37. W. Ehrmann, et al., Provenance changes between recent and glacial-time sediments in the Amundsen Sea embayment, West Antarctica: Clay mineral assemblage evidence. *Ant. Sci.* **23**, 471–486 (2011).
38. G. J. G. Paxman, et al., Reconstructions of Antarctic topography since the Eocene–Oligocene boundary. *Palaeogeogr. Palaeoclim. Palaoecol.* **535**, 109346 (2019).
39. J. J. Coenen, et al., Paleogene marine and terrestrial development of the West Antarctic Rift System. *Geophys. Res. Lett.* **47**, e2019GL085281 (2020).
40. G. J. G. Paxman, E. G. W. Gasson, S. S. R. Jamieson, M. J. Bentley, F. Ferraccioli, Long- term increase in Antarctic Ice Sheet vulnerability driven by bed topography evolution. *Geophys. Res. Lett.* **47**, e2020GL09000 (2020).
41. J. Van Breedam, P. Huybrechts, M. Crucifix, Modelling evidence for late Eocene Antarctic glaciations. *Earth Planet. Sci. Lett.* **586**, 117532 (2022).
42. M. Kageyama, et al., The PMIP4 Last Glacial Maximum experiments: Preliminary results and comparison with the PMIP3 simulations, *Clim. Past* **17**, 1065–1089 (2021).
43. The Cenozoic $CO_2$ Proxy Integration Project (Cen$CO_2$PIP) Consortium. Toward a Cenozoic history of atmospheric $CO_2$. *Science* **382**, doi:10.1126/science.adi5177 (2023).

44. C. R. Fielding, T. R. Naish, K. J. Woolfe. Facies Architecture of the CRP-3 Drillhole, Victoria Land Basin, Antarctica. *Terra Ant.* **8**, 217–224 (2001).
45. S. Galeotti, et al., Cyclochronology of the Eocene–Oligocene transition from the Cape Roberts Project-3 core, Victoria Land basin, Antarctica. *Palaeogeogr. Palaeoclimatol. Palaeoecol.* **335–336**, 84–94 (2012).
46. J. Prenzel, et al., Development and inversion of the Mesozoic Victoria Basin in Terra Nova Bay (Transantarctic Mountains) derived from thermochronological data. *Gondw. Res.* **53**, 110–128 (2018).
47. I. Sauermilch, et al., Gateway-driven weakening of ocean gyres leads to Southern Ocean cooling. *Nat. Commun.* **12**, 6465 (2021).
48. G. Uenzelmann-Neben, et al., Deep water inflow slowed offshore expansion of the West Antarctic Ice Sheet at the Eocene–Oligocene transition. *Nat. Commun. Earth Environ.* **3**, 36 (2022).
49. N. Wunderling, M. Willeit, J. F. Donges, R. Winkelmann, Global warming due to loss of large ice masses and Arctic summer sea ice. *Nat. Commun.* **11**, 5177 (2020).
50. D. Stalling, M Westerhoff, H.-C. Hege, Amira: A Highly Interactive System for Visual Data Analysis. In: Hansen, C. D. and Johnson, C. R. (eds.) The Visualization Handbook, Elsevier, The Netherlands, 749–767 (2005).
51. T. Utescher, et al., The Coexistence Approach—Theoretical background and practical considerations of using plant fossils for climate quantification. *Palaeogeogr. Palaeoclimatol. Palaeoecol.* **410**, 58–73 (2014).
52. J. I. Raine, D. C. Mildenhall, E. M. Kennedy, New Zealand fossil spores and pollen: an illustrated catalogue. 4th edition. GNS Science miscellaneous series 4, http://data.gns.cri.nz/sporepollen/index.htm (2011).
53. GBIF.org: GBIF Occurrence Download. https://doi.org/10.15468/dl.ebss8a (accessed on August 1, 2022).
54. S. E. Fick, R. J. Hijmans, WorldClim 2: new 1-km spatial resolution climate surfaces for global land areas. *Int. Journ. of Climatol.* **37**, 4302–4315 (2017).
55. G. L. Williams, H. Brinkhuis, M. A. Pearce, R. A. Fensome, J. W. Weegink, Southern Ocean and global dinoflagellate cyst events compared: Index events for the late Cretaceous–Neogene. In: Proceedings of the Ocean Drilling Program, eds. Exon, N. F., Kennett, J. P. & Malone, M. J. *Sci. Res.* **189**, 1–98 (2004).
56. C. D. Clowes, M. J. Hannah, G. J. Wilson, J. H. Wrenn, Marine palynostratigraphy and new species from the Cape Roberts Drill-holes, Victoria Land Basin, Antarctica. *Mar. Micropaleontol.* **126**, 65–84 (2016).
57. P. K. Bijl, A. J. P. Houben, A. Bruls, J. Pross, J., F. Sangiorgi, Stratigraphic calibration of Oligocene–Miocene organic-walled dinoflagellate cysts from offshore Wilkes Land, East Antarctica, and a zonation proposal. *J. Micropal.* **37**, 105–138 (2018).
58. M. J. Hannah, F. Florindo, D. M. Harwood, C. R. Fielding, CRP Science Team, Chronostratigraphy of the CRP-3 drillhole, Victoria Land Basin, Antarctica. *Terra Ant.* **8** (4), 615–620 (2001).
59. J. Weber, T. Bauersachs, L. Schwark, A multiphasic Younger Dryas cold period recorded in sediments of Lake Steisslingen, SW-Germany: A biomarker perspective. *Quat. Int.* **542**, 121–136 (2020).
60. R. A. Bourbonniere, P. A. Meyers, Sedimentary geolipid records of historical changes in the watersheds and productivities of Lakes Ontario and Erie. *Limnol. Oceanogr.* **41**, 352–455 359 (1996).
61. K. E. Peters, C. C. Walters, J. M. Moldowan, The Biomarker Guide. Cambridge University Press, 1155 p. (2004).
62. E. C. Hopmans, S. Schouten, J. S: Sinninghe Damsté, The effect of improved chromatography on GDGT-based palaeoproxies. *Org. Geochem.* **93**, 1–6 (2016).
63. E. C. Hopmans, et al., A novel proxy for terrestrial organic matter in sediments based on branched and

isoprenoid tetraether lipids. *Earth Planet. Sci. Lett.* **224**, 107–116 (2004).
64. J.-H. Kim, et al., New indices and calibrations derived from the distribution of crenarchaealisoprenoidtetraether lipids: Implications for past sea surface temperature reconstructions. *Geochim. Cosmochim. Acta* **74**, 4639–4654 (2010).
65. J.-H. Kim, et al., Holocene subsurface temperature variability in the eastern Antarctic continental margin. *Geophys. Res. Lett.* **39**, 4639–4654 (2012).
66. J. W. H. Weijers, S. Schouten, O. C. Spaargaren, J. S. Sinninghe Damsté, Occurrence and distribution of tetraether membrane lipids in soils: Implication for the use of the $TEX_{86}$ proxy and the BIT index. *Org. Geochem.* **37**, 1680–1693 (2006).
67. F. Sangiorgi, et al., Southern Ocean warming and Wilkes Land ice sheet retreat during the mid-Miocene. *Nat. Commun.* **9**, 317 (2018).
68. J. S. Sinninghe Damsté, Spatial heterogeneity of sources of branched tetraethers in shelf systems: The geochemistry of tetraethers in the Berau River delta (Kalimantan, Indonesia). *Geochim. Cosmochim. Acta* **186**, 13–31 (2016).
69. S. Schouten, et al., An interlaboratory study of $TEX_{86}$ and BIT analysis of sediments, extracts, and standard mixtures. *Geochem. Geophys. Geosys.* **14**, 5263–5285 (2013).
70. Y. G. Zhang, C. L. Zhang, X. L. Liu, K. U. Hinrichs, J. E. Noakes, Methane Index: A Tetraether archaeal lipid biomarker indicator for detecting the instability of marine gas hydrates. *Earth Planet. Sci. Lett.* **307**, 525–534 (2011).
71. J. S. Sinninghe Damsté, J. Ossebaar, S. Schouten, D. Verschuren, Distribution of tetraether lipids in the 25-ka sedimentary record of Lake Challa: Extracting reliable $TEX_{86}$ and MBT/CBT paleotemperatures from an equatorial African lake. *Quat. Sci. Rev.* **50**, 43–54 (2012).
72. S. J. Hurley, J. S. Lipp, H. G. Close, K. U. Hinrichs, A. Pearson, Distribution and export of isoprenoid tetraether lipids in suspended particulate matter from the water column of the Western Atlantic Ocean. *Org. Geochem.* **116**, 90-102 (2018).
73. K. W. R. Taylor, M. Huber, C. J. Hollis, M. T. Hernandez-Sanchez, R. D. Pancost, Re-evaluting modern and Palaeogene GDGT distributions: Implications for SST reconstructions. *Global Planet. Change* **108**, 158-174 (2013).
74. J. W. H. Weijers, S. Schouten, J. C. van den Donker, E. C. Hopmans, J. S. Sinninghe Damsté, Environmental controls on bacterial tetraether membrane lipid distribution in soils. *Geochim. Cosmochim. Acta* **71**, 703–713 (2007).
75. C. De Jonge, et al., Occurrence and abundance of 6-methyl branched glycerol dialkyl glycerol tetraethers in soils: Implications for palaeoclimate reconstruction. Geochim. Cosmochim. Acta 141, 97–112 (2014).
76. J. M. Russell, E. C. Hopmans, S. E: Loomis, J. Liang, J. S. Sinninghe Damste, Distributions of 5- and 6-methyl branched glycerol dialkyl glycerol tetraethers (brGDGTs) in East African lake sediment: Effects of temperature, pH, and new lacustrine paleotemperature calibrations. *Org. Geochem.* **117**, 56–69 (2018).
77. X. Dang, et al., Different temperature dependence of the bacterial brGDGT isomers in 35 Chinese lake sediments compared to that in soils. *Org. Geochem.* **119**, 72–79 (2018).
78. L. Wu, et al., Evaluating Zr/Rb Ratio From XRF Scanning as an Indicator of Grain-Size Variations of Glaciomarine Sediments in the Southern Ocean. *Geochem. Geophys. Geosyst.* **21**, e2020GC009350 (2020).
79. J. L. Kirschvink, The least-squares line and plane and the analysis of paleomagnetic data. *J. Royal Astr. Soc.* **62**, 699–718 (1980).
80. H. S. Knahl, L. Niu, G. Lohmann, P. Gierz, J. P. Klages, Source codes of AWIESM with interactive ice sheet model PISM. Zenodo, https://doi.org/10.5281/zenodo.10808075.
81. D. Sidorenko, et al., Evaluation of FESOM2.0 coupled to ECHAM6.3: Pre-industrial and

HighResMIP simulations. *J. Adv. Model. Earth Sy.*, 2019MS001696, https://doi.org/10.1029/2019MS001696 (2019).
82. S. Danilov, D. Sidorenko, Q. Wang, T. Jung, The Finite-volumE Sea ice–Ocean Model (FESOM2), *Geosci. Model Dev.* **10**, 765–789 (2017).
83. B. Stevens, et al., Atmospheric component of the MPI-M Earth System Model: ECHAM6. *J. Adv. Model. Earth Sy.* **5**, 146–172 (2013).
84. T. J. Raddatz, et al., Will the tropical land biosphere dominate the climate-carbon cycle feedback during the twenty-first century? *Clim. Dynam.* **29**, 565–574 (2007).
85. M. Carré, et al., High-resolution marine data and transient simulations support orbital forcing of ENSO amplitude since the mid-Holocene. *Quat. Sci. Rev.* **268**, doi:10.1016/j.quascirev.2021.107125 (2021).
86. The PISM authors. PISM, a Parallel Ice Sheet Model. https://github.com/pism/docs (2015).
87. E. Bueler, J. Brown, Shallow shelf approximation as a "sliding law" in a thermomechanically coupled ice sheet model. *J. Geophys. Res. Earth Surf.* **114**, doi:10.1029/2008JF001179 (2009).
88. R. Winkelmann, et al., The Potsdam Parallel Ice Sheet Model (PISM-PIK) – Part 1: Model description. *The Cryosphere* **5**, 715–726 (2011).
89. L. B. Stap, J. Sutter, G. Knorr, M. Starz, G. Lohmann, Transient variability of the Miocene Antarctic ice sheet smaller than equilibrium differences. *Geophys. Res. Lett.* 46, 4288–4298 (2019).
90. R. Reese, T. Albrecht, M. Mengel, X. Asay-Davis, R. Winkelmann, Antarctic sub-shelf melt rates via PICO. *The Cryosphere* **12**, 1969–1985 (2018).
91. A. Carter, T. R. Riley, C.-D. Hillenbrand, M. Rittner, Widespread Antarctic glaciation during the Late Eocene. *Earth Planet. Sci. Lett.* **458**, 49–57 (2017).
92. S. Galeotti, et al., Chapter 7 – The Eocene–Oligocene boundary climate transition: an Antarctic perspective. In: Florindo, F., Siegert, M., De Santis, L. & Naish, T. (eds.) Antarctic Climate Evolution (Second Edition), Elsevier, 297–361 (2022).
93. J. I. Raine, R. A. Askin, Terrestrial palynology of Cape Roberts Project drillhole CRP-3, Victoria Land Basin, Antarctica. *Terra Ant.* **8**, 389–400 (2001).
94. D. J. Cantrill, Early Oligocene Nothofagus from CRP-3, Antarctica: Implications for the Vegetation History. *Terra Ant.* **8**, 401–406 (2001).
95. B. Duncan, "Cenozoic Antarctic climate evolution based on molecular and isotopic biomarker reconstructions from geological archives in the Ross Sea region". Thesis, Victoria University of Wellington (2017).
96. B. Duncan, et al., Climatic and tectonic drivers of late Oligocene Antarctic ice volume. *Nat. Geosci.* **15**, 819–825 (2022).
97. F. S. Hoem, et al., Temperate Oligocene surface ocean conditions offshore of Cape Adare, Ross Sea, Antarctica. *Clim. Past* **17**, 1423–1442 (2021).
98. E. J. Tibbett, et al., Late Eocene Record of Hydrology and Temperature From Prydz Bay, East Antarctica. *Paleoceanography* **36**, e2020PA004204 (2021).
99. K. Birkenmajer, E. Zastawniak, Late Cretaceous-early Tertiary floras of King George Island, West Antarctica: their stratigraphic distribution and palaeoclimatic significance. *Geol. Soc., London, Spec. Publ.* **47**, 227–240 (1989).
100. J. Plancq, E. Mattioli, B. Pittet, L. Simon, V. Grossi, Productivity and sea-surface temperature changes recorded during the late Eocene–early Oligocene at DSDP Site 511 (South Atlantic). *Palaeogeogr. Palaeoclim. Palaeoecol.* **407**, 34–44 (2014).
101. A. J. P. Houben, P.K. Bijl, A. Sluijs, S. Schouten, H. Brinkhuis, Late Eocene Southern Ocean Cooling and Invigoration of Circulation Preconditioned Antarctica for Full-Scale Glaciation. *Geochem. Geophys. Geosys.* **20**, 2214–2234 (2019).
102. J. G. Prebble, J. I. Raine, P. J. Barrett, M. J. Hannah, Vegetation and climate from two Oligocene

glacioeustatic sedimentary cycles (31 and 24 Ma) cored by the Cape Roberts Project, Victoria Land Basin, Antarctica. *Palaeogeogr. Palaeoclimatol. Palaeoecol.* **231**, 41–57 (2006).
103. N. Thompson, et al., Vegetation change across the Drake Passage region linked to late Eocene cooling and glacial disturbance after the Eocene–Oligocene transition. *Clim. Past* **18**, 209–232 (2022).
104. M. Amoo, U. Salzmann, M. J. Pound, N. Thompson, P. K. Bijl, Eocene to Oligocene vegetation and climate in the Tasmanian Gateway region controlled by changes in ocean currents and pCO2. *Clim. Past* **18**, 525–546 (2022).
105. P. K. Bijl, et al., Maastrichtian-Rupelian paleoclimates in the southwest Pacific – a critical evaluation of biomarker paleothermometry and dinoflagellate cyst paleoecology at Ocean Drilling Program Site 1172. *Clim. Past* **17**, 2393–2425 (2021).
106. J. D. Hartman, et al., Paleoceanography and ice sheet variability offshore Wilkes Land, Antarctica – Part 3: Insights from Oligocene–Miocene $TEX_{86}$-based sea surface temperature reconstructions. *Clim. Past* **14**, 1275–1297 (2018).
107. A. Paytan, et al., A 35-million-year record of seawater stable Sr isotopes reveals fluctuating global carbon cycle. *Science* **371**, 1346–1350 (2021).
108. A. O. Nier, The isotopic constitution of strontium, barium, bismuth, thallium and mercury. *Phys. Rev.* **54**, 275 (1938).
109. J. M. McArthur, R. J. Howarth, T. R. Bailey, Strontium isotope stratigraphy: LOWESS version 3: Best fit to the marine Sr-isotope curve for 0–509 Ma and accompanying look-up table for deriving numerical age. *J. Geol.* **109**, 155–170 (2001).

*Corresponding author*
All correspondence and requests for materials should be addressed to J. P. Klages (Johann.Klages@awi.de).

**Acknowledgements**
We thank captain, crew and scientists of RV *Polarstern* Expedition PS104, as well as the MARUM-*MeBo70* team for their support. V. Afanasyeva, J. E. Arndt, C. Gebhardt, Y. Najman, P. Simões Pereira, F. Riefstahl, M. Scheinert, and M. Zundel were part of the Science Team of Expedition PS104 and are thanked for their help on board and in the lab. S. Wiebe, R. Fröhlking, V. Schumacher, N. Lensch, M. Arevalo, M. Kuck, D. Diekstall, M. Seebeck, and R. Cordelair are thanked for technical support on board and in the lab, respectively. The *Klinikum Bremen-Mitte* (A.-J. Lemke and C. Tiemann, *Gesundheit Nord* Bremen) is acknowledged for providing facilities for computed core tomographies, and M. Köhler (MKfactory, Germany) as well as C. Schott (University of Bremen, Germany) for preparing the thin sections. S.S.R. Jamieson (University of Durham, UK) is thanked for advice on initial ice pre-settings for the model. We are grateful to K. Worm and C. Rolf (LIAG Hannover, Service Area Grubenhagen) for providing access to the long-core cryogenic magnetometer. We further thank B. Diekmann for commenting on an earlier version of this manuscript and S. Schumacher for PANGAEA data curation.
**Funding:** The operation of the MARUM-MeBo70 Sea Floor Drill Rig was funded by the Alfred Wegener Institute (AWI) through its Research Program PACES II Topic 3 and grant no. AWI_PS104_001, the MARUM Center for Marine Environmental Sciences, the British Antarctic Survey through its Polar Science for Planet Earth programme, and the Natural Environmental Research Council (NERC) funded UK IODP programme. J.P.K, K.G., G.K., G.L., H.S.K., L.N., P.G., J.M., G.N., G.U.-N., and O.E. were funded by the AWI PACES II and the Helmholtz Association "Changing Earth – Sustaining our future" programme. J.P.K. and J.M. were additionally funded through the Helmholtz Association (PD-201 & VH-NG-1101). C.-D.H., R.D.L. and J.A.S. were funded by NERC. UK IODP funded participation of T.v.d.F. and S.M.B. in expedition PS104. J.T. was funded through the Cluster of Excellence "The Ocean Floor – Earth's Uncharted Interface" at the University of Bremen. S.S. received funding for *Bolboforma* investigations from the Swiss National Science Foundation (grant number 200020_201106). **Author contributions:** J.P.K. led the study and together with C.-D.H., S.M.B., U.S., and K.G., conceived the idea for the study and wrote the manuscript. Ti.F., J.P.K, T.B., C.-D.H., S.M.B., J.A.S., K.G., T.v.d.F., W.E., O.E. and H.P. collected the cores. J.P.K, C.-D.H., T.B. and G.K. undertook the sedimentological, U.S. and S.M.B. the micropaleontological and biostratigraphic analyses, and G.S. and S.S. the identification and interpretation of calcareous microfossils. T.B. and G.K. conducted the XRF scanning and processing of the cores. G.K. and J.P.K. carried out the grain-size and -shape analyses. J.T. led the CT scanning, processing, and visualization. J.T., F.J.R.-T. and J.P.K. interpreted the CT data. J.M. and T.Ba. performed the biomarker analyses. T.F. conducted the paleomagnetic measurements. A.E. led the strontium isotope dating. G.N., G.K., J.P.K., and C.S. investigated the thin sections. W.E. analysed the clay mineral assemblages. G.L., H.S.K., P.G. and L.N. undertook the modelling with AWI-ESM 2.1 and PISM. K.H., K.G., F.L., and A.L. helped improving the paleo-topography as boundary condition for the model. J.P.K., T.B., C.-D.H., S.M.B., T.F., W.E., J.A.S., O.E., H.P., R.D., and T.A.R. helped sampling and scanning the cores. K.G., G.U.-N. and R.D.L. undertook the seismic site survey. All members of the Expedition PS104 Science Team helped in pre-site survey investigations, core recovery, on-board analyses and/or shore-based measurements. K.G., G.K., R.D.L., G.U.-N., T.B. and C.-D.H. acquired funding, proposed, and planned RV *Polarstern* expedition PS104. All co-authors commented on the manuscript and provided input to its final version. **Competing interests:** Authors declare that they have no competing interests. **Data and materials availability:** All data are available online in the Data Base for Earth and Environmental Science (PANGAEA) (*26, 27*). The source codes of the Alfred Wegener Institute-Earth System Model 2.1 (AWI-ESM 2.1) and the Parallel Ice Sheet Model (PISM) are available online in the Data Base Zenodo (*80*).

**Science Team of Expedition PS104**

Afanasyeva, V., VNIIOkeangeologie, St. Petersburg, Russia
Arndt, J. E., Departamento de Geografía, University of Concepción, Concepción, Chile
Dziadek, R., Alfred-Wegener-Institut, Helmholtz-Zentrum für Polar- und Meeresforschung, Bremerhaven, Germany
Gebhardt, C., Alfred-Wegener-Institut, Helmholtz-Zentrum für Polar- und Meeresforschung, Bremerhaven, Germany
Najman, Y., Lancaster Environment Centre, Lancaster University, Lancaster, United Kingdom
Simões Pereira, P., Institute of Geology, University of Innsbruck, Innsbruck, Austria
Riefstahl, F., Alfred-Wegener-Institut, Helmholtz-Zentrum für Polar- und Meeresforschung, Bremerhaven, Germany
Ronge, T.A., International Ocean Discovery Program, Texas A&M University, College Station, TX, USA
Scheinert, M., Technische Universität Dresden, Dresden, Germany
Zundel, M., University of Bremen, Faculty of Geosciences, Bremen, Germany

**Supplementary Materials**

Materials and Methods
Figures (S1-S11)
Tables (S1-S6)
References (*50-109*)
Movie (S1)

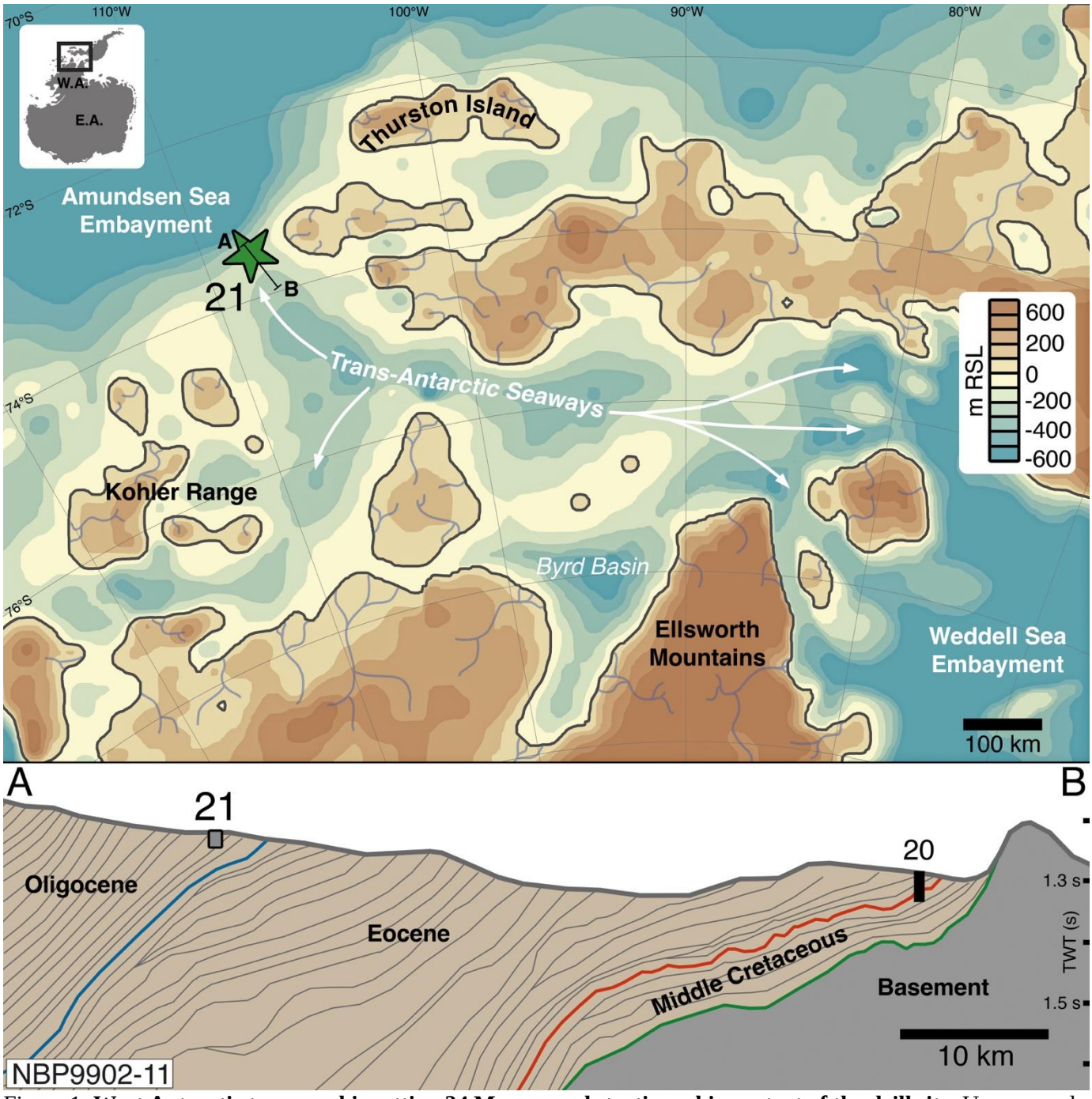


Figure 1: **West Antarctic topographic setting 34 Ma ago and stratigraphic context of the drill site.** Upper panel: Map of the West Antarctic archipelago between the Amundsen Sea Embayment and Weddell Sea at the time of the Early Oligocene Glacial Maximum (EOGM) with MeBo drill site PS104_21 (green star) based on the reconstructed 34 Ma minimum bed topography from ref. *38*. Locations of MeBo drill site PS104_21 (green star) and the seismic profile NBP9902-11 (line A–B) presented in the lower panel are also shown. Positions of rivers are hypothetical and based on our interpretation of the paleoenvironmental conditions for the deposition of the PS104_21 sediments, inferred from micropaleontological and biomarker analyses (see text). m RSL: Relative sea level (in metres). The inset in upper left corner indicates locations of West Antarctica (W.A.), East Antarctica (E.A.), and the study area. Lower panel: Interpretation of seismic profile NBP9902-11 (*19, 21*) with projected position (grey) of MeBo site PS104_21 and position of MeBo site PS104_20 (*20*), which is included for further context. TWT (s): Two-way-travel time (in seconds).

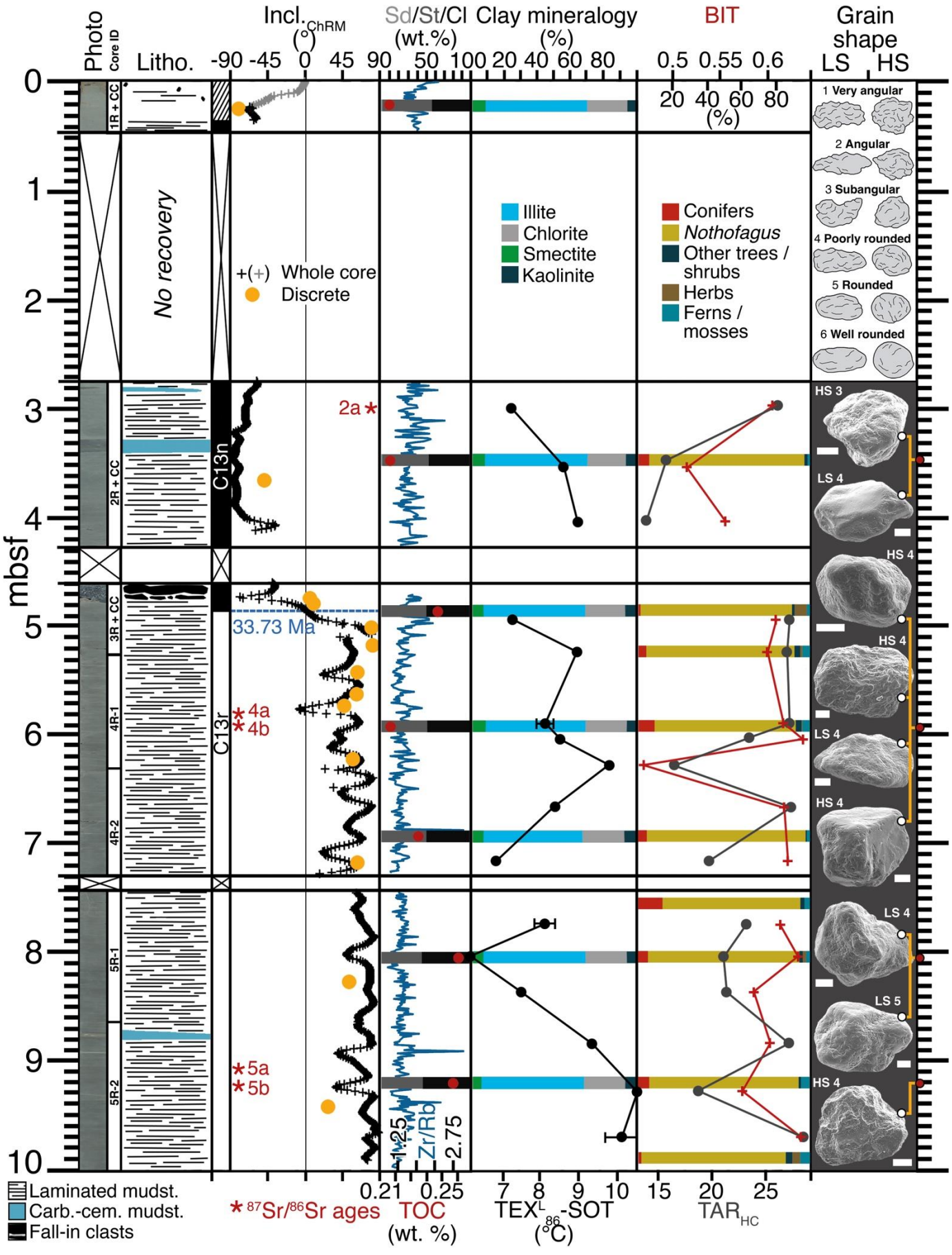
Photo
Core ID
Litho.
Incl.ChRM (°)
Sd/St/Cl (wt.%)
Clay mineralogy (%)
BIT
Grain shape
LS HS
1 Very angular
2 Angular
3 Subangular
4 Poorly rounded
5 Rounded
6 Well rounded
Illite
Chlorite
Smectite
Kaolinite
Conifers
Nothofagus
Other trees / shrubs
Herbs
Ferns / mosses
+(+) Whole core
Discrete
No recovery
1R + CC
2R + CC
3R + CC
4R-1
4R-2
5R-1
5R-2
C13n
C13r
33.73 Ma
2a
4a
4b
5a
5b
HS 3
LS 4
HS 4
LS 4
HS 4
LS 4
LS 5
HS 4
mbsf
Laminated mudst.
Carb.-cem. mudst.
Fall-in clasts
*87Sr/86Sr ages
TOC (wt. %)
Zr/Rb
TEXL86-SOT (°C)
TARHC

Figure 2: **Multi-proxy results from MeBo drill site 21-3 (*27*).** Core photos, lithology, magnetic inclination data (measured on whole cores and discrete samples), various environmental proxies, and Scanning Electron Microscope (SEM) images of sand-sized quartz grains (sample depths indicated by yellow brackets) from cores 1R to 5R of hole PS104_21-3. The MARUM-MeBo70 sea floor drill rig penetrated 10 m into the seabed and recovered 7.34 m of core (73.4 %). A ~4 cm thin drape of Holocene unconsolidated sandy mud was recovered just beneath the seafloor, while a ~1.1 m long sequence of bioturbated to laminated mud and sandy mud overlying structureless diamicton – probably reflecting deposition since the Last Glacial Maximum (LGM) – was retrieved in hole PS104_21-2 and gravity core PS104_21-1 from the same location. The sediments below the Holocene sandy mud in hole PS104_21-3 consist of ~7.30 m of laminated semi-lithified mud and mudstone of earliest Oligocene age. Two carbonate-cemented mudstone beds occur at ~8.78–8.74 mbsf and ~3.33–3.23 mbsf. Sampling depths and associated sample numbers for strontium isotope ($^{87}Sr/^{86}Sr$) dating are indicated by red stars with results given in Extended Data Table 1 and Extended Data Fig. 2. C13r & C13n: Magnetic polarity chrons; $Incl._{ChRM}$: Inclination values of characteristic remanent magnetization (see 'Materials and Methods' in Supplementary Materials); Sd/St/Cl: Sand/Silt/Clay; Zr/Rb: Zirconium–Rubidium ratio [= grain-size proxy]; TOC: Total Organic Carbon; clay mineral assemblages; $TEX^{L}_{86}$-SOT: $TEX^{L}_{86}$ Sub-Surface Ocean Temperatures (error bars indicate analytical error for replicated samples); palynomorph percentages; BIT: Branched and Isoprenoid Tetraether index; $TAR_{HC}$: Ratio of Terrestrial and Aquatic-sourced hydrocarbons; LS: Low sphericity; HS: High sphericity; mbsf: meters below sea floor.

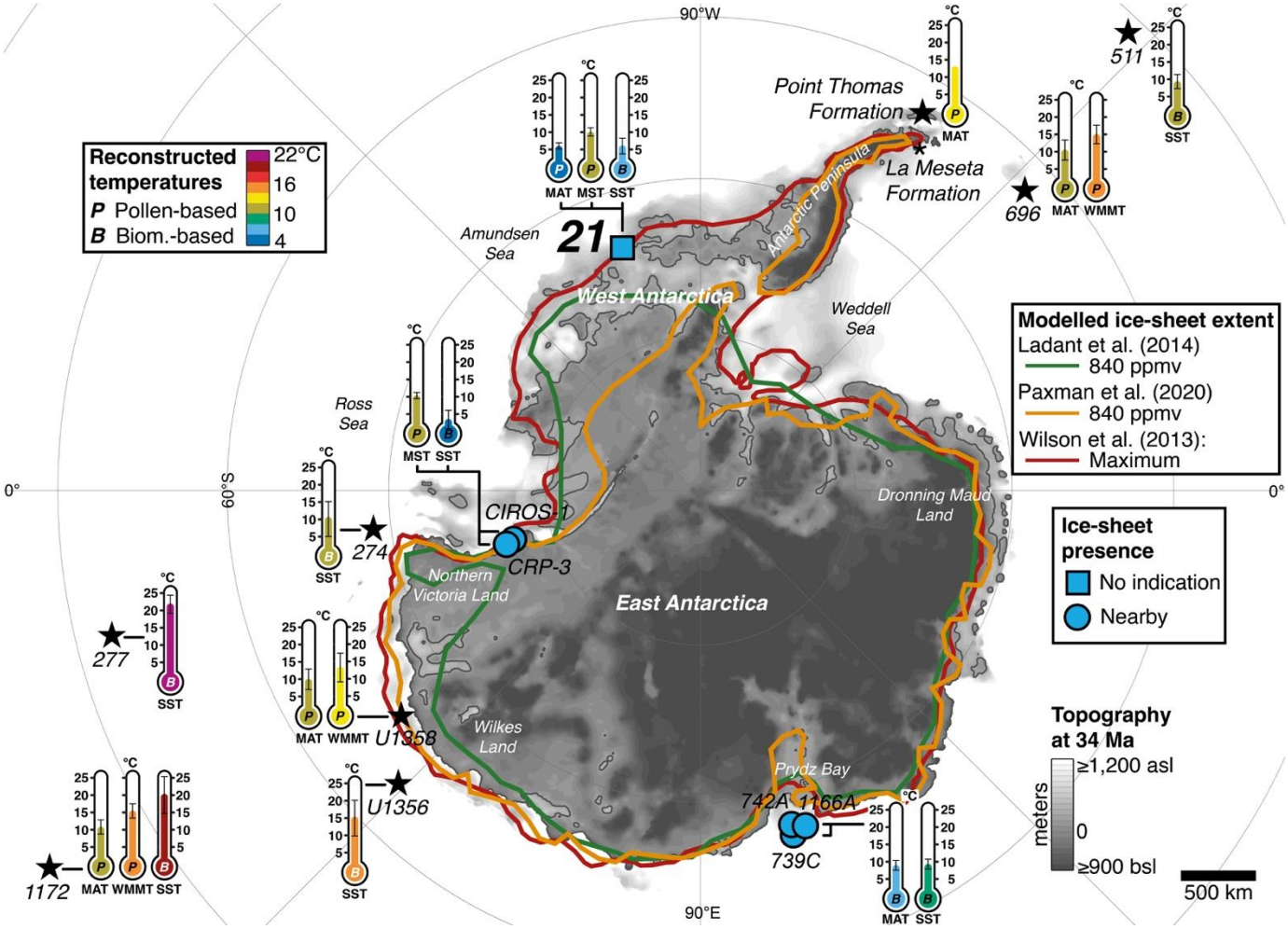


Figure 3: **Circum-Antarctic paleo-environmental data evidence and previous modeling scenarios for earliest Oligocene Antarctic ice sheet-extent.** Existing earliest Oligocene (33.9–31 Ma) data records around Antarctica for terrestrial and sea-surface temperatures, and ice presence (Point Thomas and La Meseta formations are exposed on land). Available pollen- (*P*) or biomarker-based (*B*) temperature proxy results are shown separately for each site (MAT: Mean annual temperature; MST: Mean summer temperature; WMMT: Warmest mean month temperature; SST: Sea-surface temperature) and indicate coldest values including analytical uncertainties in the 33.9–31 Ma period. Sites with available data for ice presence/absence are marked by the blue icons referenced within the figure, while all other sites are indicated by black stars. Only the La Meseta Formation is indicated by an asterisk since ice-sheet presence is under debate (*14*, *15*). The green, red, and orange outlines refer to different modeled ice-sheet extents at the EOGM (*3*, *7*, *40*). All data visualized here are listed in more detail and referenced in Table S6. The minimum topography reconstruction from ref. *38* was used (asl: above sea level; bsl: below sea level).

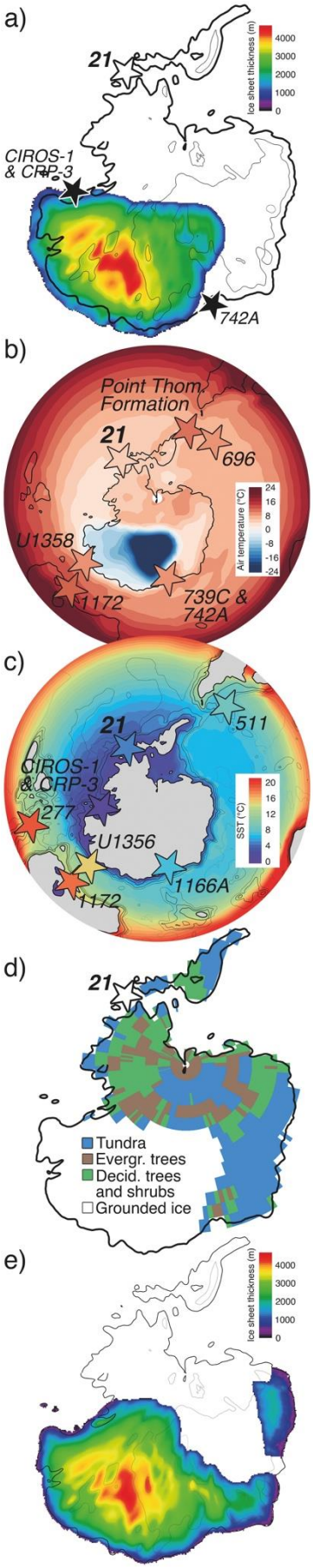
a)
21
CIROS-1
& CRP-3
742A
Ice sheet thickness (m)
4000
3000
2000
1000
0
b)
Point Thom
Formation
21
696
U1358
1172
739C &
742A
Air temperature (°C)
24
16
8
0
-8
-16
-24
c)
21
511
CIROS-1
& CRP-3
277
U1356
1166A
1172
SST (°C)
20
16
12
8
4
0
d)
21
Tundra
Evergr. trees
Decid. trees
and shrubs
Grounded ice
e)
Ice sheet thickness (m)
4000
3000
2000
1000
0

Figure 4:
**Results of ice sheet and Earth System modelling compared to paleo-data records.** Simulated Antarctic environment for 840 ppmv (3x PI [= pre-industrial]) atmospheric carbon dioxide ($CO_2$) forcing compared to available data. Ice-sheet configuration 200,000 years after ice-free conditions (panel a) with the corresponding EOGM climate showing air temperatures at 2 m height (panel b), sea-surface temperature (panel c), and vegetation cover (panel d; Evergr.: evergreen; Decid.: deciduous). Panel e shows ice-sheet configuration under 2x PI $CO_2$ conditions (cf. Fig. S6). Sites indicating ice presence in panel a) are highlighted by filled black stars, whereas white star with a black outline marks Site PS104_21 without indication for glacial ice. Stars in panels b) and c) indicate the locations of drill sites providing surface air (MATs) and sea-surface temperatures (SSTs), respectively, with their colour fill indicating the reconstructed temperature (Fig. 3; Table S6). Colours in panel a) refer to ice thickness above bedrock and black isolines indicate the minimum 34 Ma bed topography reconstruction (*38*).